ARL-TR-8753 ● AUG 2019

DEVCOM
ARMY RESEARCH LABORATORY

Approach for Understanding Range Extension of Gliding Indirect Fire Munitions

by Joshua T Bryson, Joseph D Vasile, Ilmars Celmins, and Frank E Fresconi

NOTICES

Disclaimers

The findings in this report are not to be construed as an official Department of the Army position unless so designated by other authorized documents.

Citation of manufacturer's or trade names does not constitute an official endorsement or approval of the use thereof.

Destroy this report when it is no longer needed. Do not return it to the originator.

ARL-TR-8753 ● AUG 2019

Approach for Understanding Range Extension of Gliding Indirect Fire Munitions

by Joshua T Bryson, Joseph D Vasile, Ilmars Celmins, and Frank E Fresconi
Weapons and Materials Research Directorate, CCDC Army Research Laboratory

REPORT DOCUMENTATION PAGE						*Form Approved* *OMB No. 0704-0188*
Public reporting burden for this collection of information is estimated to average 1 hour per response, including the time for reviewing instructions, searching existing data sources, gathering and maintaining the data needed, and completing and reviewing the collection information. Send comments regarding this burden estimate or any other aspect of this collection of information, including suggestions for reducing the burden, to Department of Defense, Washington Headquarters Services, Directorate for Information Operations and Reports (0704-0188), 1215 Jefferson Davis Highway, Suite 1204, Arlington, VA 22202-4302. Respondents should be aware that notwithstanding any other provision of law, no person shall be subject to any penalty for failing to comply with a collection of information if it does not display a currently valid OMB control number. **PLEASE DO NOT RETURN YOUR FORM TO THE ABOVE ADDRESS.**						
1. REPORT DATE *(DD-MM-YYYY)* August 2018		**2. REPORT TYPE** Technical Report				**3. DATES COVERED (From - To)** 1 September 2018–30 November 2018
4. TITLE AND SUBTITLE Approach for Understanding Range Extension of Gliding Indirect Fire Munitions						**5a. CONTRACT NUMBER**
						5b. GRANT NUMBER
						5c. PROGRAM ELEMENT NUMBER
6. AUTHOR(S) Joshua T Bryson, Joseph D Vasile, Ilmars Celmins, and Frank E Fresconi						**5d. PROJECT NUMBER**
						5e. TASK NUMBER
						5f. WORK UNIT NUMBER
7. PERFORMING ORGANIZATION NAME(S) AND ADDRESS(ES) CCDC Army Research Laboratory* ATTN: FCDD-RLW-LE Aberdeen Proving Ground, MD 21005-5066						**8. PERFORMING ORGANIZATION REPORT NUMBER** ARL-TR-8753
9. SPONSORING/MONITORING AGENCY NAME(S) AND ADDRESS(ES)						**10. SPONSOR/MONITOR'S ACRONYM(S)**
						11. SPONSOR/MONITOR'S REPORT NUMBER(S)
12. DISTRIBUTION/AVAILABILITY STATEMENT Approved for public release; distribution is unlimited.						
13. SUPPLEMENTARY NOTES * As of February 2019, the US Army Research Laboratory has been renamed the US Army Combat Capabilities Development Command Army Research Laboratory (CCDC ARL).						
14. ABSTRACT This report formulates an approach for understanding range extension of gliding indirect fire munitions equipped with enhanced lifting surfaces. The key elements consist of accurate aerodynamic characterization, flexible analytical tools, and high-fidelity flight simulations. Several techniques are integrated to accurately characterize the aerodynamics. Analytical tools were developed that accommodate rapid alteration of the enhanced lifting surface characteristics to recommend optimal configurations, which are examined in flight simulation. This framework is demonstrated using a munition concept with deployable aerodynamic surfaces. Results highlight the importance of lift-to-drag and the optimal trim angle induced by the control mechanism on range maximization. The generalized approach outlined in this report can be applied to specific system constraints such as launch conditions (e.g., initial velocity and angle), munition size/weight, and sub-system allocation (e.g., warhead volume) to inform technical decisions such as balancing flight performance and design complexity.						
15. SUBJECT TERMS gun-launched munitions, gliding munitions, aerodynamic design, range extension, optimal design						
16. SECURITY CLASSIFICATION OF:			**17. LIMITATION OF ABSTRACT**	**18. NUMBER OF PAGES**		**19a. NAME OF RESPONSIBLE PERSON** Joshua T Bryson
a. REPORT Unclassified	**b. ABSTRACT** Unclassified	**c. THIS PAGE** Unclassified	UU	40		**19b. TELEPHONE NUMBER (Include area code)** 410-306-1939

Standard Form 298 (Rev. 8/98)
Prescribed by ANSI Std. Z39.18

Contents

List of Figures iv

List of Tables v

Acknowledgments vi

1. Introduction 1

2. Munition Concept 2

3. Flight Dynamics and Aerodynamics Models 4

4. Aerodynamic Characterization 5

5. Aerodynamic Analysis of Wing 16

5.1 Wing Effect on Lift-to-Drag Ratio 16

5.2 Wing Effect on Static Margin 18

5.3 Effect of Wing Center of Pressure on Static Margin 19

5.4 Effect of Wing on Trim Angle 20

5.5 Optimized Wing Size and Location 22

6. Flight Simulation 23

7. Conclusion 25

8. References 27

List of Symbols, Abbreviations, and Acronyms 30

Distribution List 32

List of Figures

Fig. 1 Projectile concept used in this analysis, showing the nominal wing size and location. Dimensions are given in calibers. 3

Fig. 2 Geometry sketch of projectile concept modeled in MissileLab and executed in Missile DATCOM 6

Fig. 3 Contour of simulated non-dimensional streamwise velocity superimposed with the computational domain (Cart3D) 7

Fig. 4 Instrumented model mounted in WT facility test section 8

Fig. 5 Normal force coefficient (a, c, e) and pitching moment coefficient (b, d, f) of B (a–b), BF (c–d), and BFWC (e–f) configurations at Mach 0.2 from WT only, CE CFD only, SEAP only, and blended (SEAP, CE CFD, and WT) data 10

Fig. 6 Zeroth-order coefficient of axial force for B (a), BF (b), and BFWC (c) configurations from SEAP, CE CFD, WT only, and blended (SEAP, CE CFD, and WT) data across Mach number. 12

Fig. 7 First-order coefficient of static normal force and static pitching moment for BF and BFWC configurations from SEAP, CE CFD, WT only, and blended (SEAP, CE CFD, and WT) data across Mach number 13

Fig. 8 Lift-to-drag ratio for the BFC, the wing alone, and the BFWC for several wing sizes at Mach 0.5. The optimal angles of attack corresponding to the highest lift-to-drag ratios for each configuration are marked with diamonds. 17

Fig. 9 Static margin of BF and BFWC configurations for varying α............ 18

Fig. 10 Static margin at α=3° across Mach for the BFC, for the wing alone, and for the BFWC. Increasing the wing effect decreases the stability. 19

Fig. 11 Effect of shifting wing CP on wing static margin and static margin of BFWC. Shifting the wing CP toward the nose decreases the total stability. 20

Fig. 12 Static pitching moment contributions from the BFW, from canards alone with +5° deflection, and the combined BFWC for Mach 0.5. The steady-state trim angle of attack of 3.5° is found where the total static pitching moment is zero, as indicated with a diamond. 21

Fig. 13 BFWC static pitching moment at Mach 0.5 for nominally sized wings acting on the body at different CPs, with +5° canard deflection. Steady state trim angles of attack of 3.5°, 3.9°, and 4.2° are indicated with diamonds. 21

Fig. 14 Lift-to-drag ratio at steady-state trim angle of attack, plotted as a function of wing size and center of pressure at Mach 0.5. The nominal wing design is shown with a blue dot. 22

Fig. 15 Range as a function of launch angle for several configurations. Optimal launch angles for each are highlighted with a diamond........ 23

Fig. 16 Trajectories for configurations with the optimized wing designs described in Table 7 24

List of Tables

Table 1 Projectile mass properties 3

Table 2 Aerodynamic data set for B 14

Table 3 Aerodynamic data set for BF 15

Table 4 Aerodynamic data set for wing surface only 15

Table 5 Aerodynamic data set for single canard blade 16

Table 6 Optimal wing designs 23

Table 7 Best range of optimized munition configurations............................... 24

Acknowledgments

The authors are grateful to the scientists, engineers, and technicians from the Edgewood Chemical and Biological Center at Aberdeen Proving Ground for conducting wind-tunnel experiments. This work was supported in part by a grant of high-performance computing time from the US Department of Defense (DOD) High Performance Computing Modernization program at the Army Research Laboratory DOD Supercomputing Resource Center (DSRC), Aberdeen Proving Ground, Maryland, and the US Army Engineer Research and Development Center DSRC, Vicksburg, Mississippi.

1. Introduction

The primary motivation for this research is to extend the range of indirect fire munitions, which is an active area of research for the US Army. Munition range can be extended primarily through enhancing propulsion by increasing the amount and effectiveness of energetic material and by improving aerodynamics to decrease drag and increase lift. Advanced propulsion technologies are currently under investigation for both rocket- and gun-launched munitions. Additionally, range extension for gun-launched systems can be obtained by lengthening the gun tube (e.g., from 39 calibers to 52 calibers) to accelerate the projectile for a longer period of time, using larger bore guns to launch smaller diameter projectiles through the use of a sabot (e.g., US Army M829 family), or adding a rocket motor for post-launch propulsion. Understanding of the gun-launch environment is critical to ensure survivability of components.[1,2] Minnicino et al.[3] explore effects of state-of-the-art propellants, tube length, and sabot launch on range for gun-launched artillery systems.

For a fixed propulsive energy, the range can be extended by gliding the flight vehicle with improved aerodynamic configurations potentially consisting of surfaces that may need to be packaged and deployed for tube launch. Costello[4] used high-fidelity dynamic modeling with a low-order aerodynamic characterization in a parametric study to introduce the benefit of canards in extending the range of gun-launched artillery. Fresconi[5] applied similar tools to investigate a more general munition configuration and control mechanism, included rocket motors, and developed flight controllers to deal with the cross-range drift that accompanies slowly-rolling munitions flying at angle of attack. These results demonstrated that rocket motors should activate mid-way between launch and apogee to optimize atmospheric density effects on thrust and drag. More detailed maneuver schemes (e.g., rolling airframes, bank-to-turn, and skid-to-turn) and actuation technologies (e.g., voice coils and servo-mechanisms) were examined in gliding flight investigations by Fresconi et al.[6] This study indicated that a specific launch angle and deployment/glide time exists for maximum glide range. Four-axis control actuation of a vehicle flying in a skid-to-turn arrangement appeared to provide the best packaging-flight performance. Low static margin was also desirable but this study showed how dynamic instabilities such as those produced by side moments could become more problematic at low static stability. These results were underpinned by extensive aerodynamic characterization from semi-empirical aerodynamic prediction (SEAP), computational fluid dynamics (CFD), wind tunnel (WT), and free-flight (spark range and onboard sensor) sources.[7] These investigations led to successful demonstration of range extension and closed-loop guidance of indirect fire munitions,[8,9] but did not specifically consider high angle of attack phenomenon such as flow separation when optimizing the vehicle configuration for maneuverability. Fresconi et al.[10] conducted free-flight experiments across a range of angle of attack but were unable to obtain enough data at aerodynamic angles where canard effectiveness suffered due to flow separation.

Past work has addressed different aspects fundamental to understanding and developing gliding flight technology for indirect fire munitions. The goals of this work are to formulate a more comprehensive approach for understanding range extension of gliding indirect fire munitions equipped with enhanced lifting surfaces and to identify 1) the critical components of analysis and 2) the critical technologies that limit performance. This framework is demonstrated on a gun-launched artillery munition concept featuring wings.

This report is organized as follows: 1) a physical description of the munition is provided, 2) the flight dynamic model and aerodynamic model are described, 3) the aerodynamic characterization of various munition configurations are presented, 4) the effect of modifications to the enhanced lifting surfaces are analyzed, 5) flight simulation results are presented for a range of wing sizes and locations, and 6) the key components of the approach and critical technologies limiting flight performance are summarized.

2. Munition Concept

A generic aerodynamically stabilized munition concept, with fins, a wing, and canards, as shown in Fig. 1, is the focus of this study. All aerodynamic lifting surfaces (fins, canards, wings) stow into the body at launch. For this study, the projectile is sized to 155 mm diameter, with estimated mass properties obtained from solid modeling given in Table 1. The aerodynamic surfaces are flat plates with thickness of approximately 1.6 mm. The eight fins are fixed with no cant, and are sized to stabilize the flight body at speeds below Mach 2.7. The base has a 7°, 0.16 caliber long boattail to reduce drag. The wing is fixed at 0° angle of attack relative to the body, and the canards have a ±10° deflection angle range of motion.

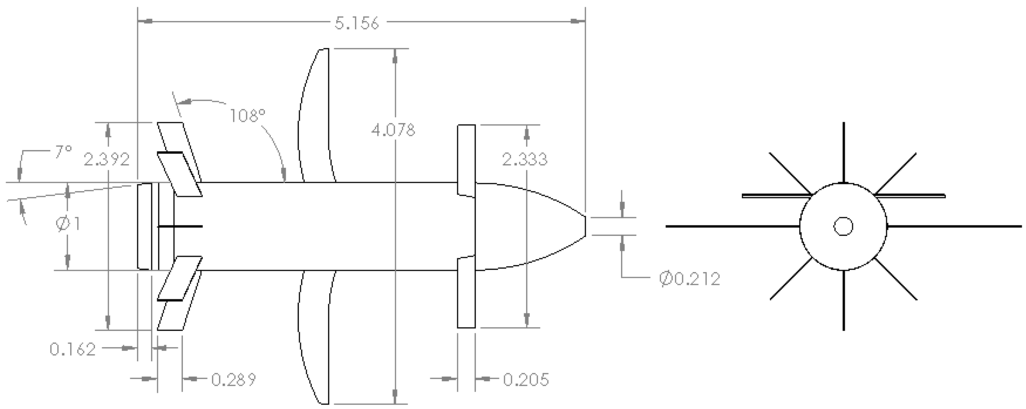

Fig. 1 Projectile concept used in this analysis, showing the nominal wing size and location. Dimensions are given in calibers.

Table 1 Projectile mass properties

Parameter	Symbol	Value	Units
Diameter	D	155	mm
Length	L	800	mm
Center of gravity	CG	2.58	calibers (from nose)
Mass	m	42.6	kg
Axial moment of inertia	I_{xx}	0.11	kg m^2
Transverse moments of inertia	$I_{yy}=I_{zz}$	9.02	kg m^2

This research is intended to understand the relationship between munition configuration and range extension. Specific physical dimensions and mass properties of the concept munition given in this paper are likely to change as this understanding matures through further technology development and experimentation. Some or all of the aerodynamic surfaces may be modified in planform or cross section (e.g., from flat plates to an airfoil profile), the body length may change, and the nose shape may be revisited in future research. This report, however, is focused on understanding how the lifting surface influences the range extension.

Operational employment of this munition concept uses a lofted trajectory achieved by a high launch angle. The projectile is launched from a smooth-bore gun tube or from a rifled gun tube using a slip-band obturator. As the projectile is not spin-stabilized, the fins deploy immediately after launch. Near apogee, the wings and canards deploy and the canards deflect to pitch the projectile nose up to increase the total angle of attack and generate lift from the body and lifting surfaces.

Larger wings generate greater lift and are expected to increase range, but are more challenging to stow and deploy, and to maintain rigidity and structural integrity.

This analysis investigates the effect of changing the wing size from the nominal design shown in Fig. 1 to understand the relationship between lifting surface effects and range extension, and to inform future technical decisions balancing munition performance and overall design complexity.

Throughout this study, the mass properties were held fixed, while the components of the aerodynamic forces and moments due to the wing are varied. These aerodynamic modifications provide an opportunity to approximate the effect of changing the wing size and location. This enables a generalized analysis based on wing characteristics applied to a munition with consistent mass properties. The term "wing size" is used in this report to refer to the magnitude of the aerodynamic forces and moments, not necessarily the physical dimensions.

3. Flight Dynamics and Aerodynamics Models

The projectile is modeled as a rigid body with 12 states: the center-of-gravity position $[x \quad y \quad z]^T$, the Euler angles describing body attitude $[\varphi \quad \theta \quad \psi]^T$, as well as the body translational velocity $[u \quad v \quad w]^T$ and rotational velocity $[p \quad q \quad r]^T$. The nonlinear, six-degree-of-freedom kinematic and dynamic model for the projectile flight is as follows:[11,12]

$$\begin{bmatrix} \dot{x} \\ \dot{y} \\ \dot{z} \end{bmatrix} = \begin{bmatrix} \cos\theta\cos\psi & \sin\varphi\sin\theta\cos\psi - \cos\varphi\sin\psi & \cos\varphi\sin\theta\cos\psi + \sin\varphi\sin\psi \\ \cos\theta\sin\psi & \sin\varphi\sin\theta\sin\psi + \cos\varphi\cos\psi & \cos\varphi\sin\theta\sin\psi + \sin\varphi\cos\psi \\ -\sin\theta & \sin\varphi\cos\theta & \cos\varphi\cos\theta \end{bmatrix} \begin{bmatrix} u \\ v \\ w \end{bmatrix} \tag{1}$$

$$\begin{bmatrix} \dot{\varphi} \\ \dot{\theta} \\ \dot{\psi} \end{bmatrix} = \begin{bmatrix} 1 & \sin\varphi\tan\theta & \cos\varphi\tan\theta \\ 0 & \cos\varphi & -\sin\varphi \\ 0 & \dfrac{\sin\varphi}{\cos\theta} & \dfrac{\cos\varphi}{\cos\theta} \end{bmatrix} \begin{bmatrix} p \\ q \\ r \end{bmatrix} \tag{2}$$

$$\begin{bmatrix} \dot{u} \\ \dot{v} \\ \dot{w} \end{bmatrix} = \begin{bmatrix} 0 & r & -q \\ -r & 0 & p \\ q & -p & 0 \end{bmatrix} \begin{bmatrix} u \\ v \\ w \end{bmatrix} + \frac{1}{m} \begin{bmatrix} F_X \\ F_Y \\ F_Z \end{bmatrix} + \begin{bmatrix} -\sin\theta \\ \sin\varphi\cos\theta \\ \cos\varphi\cos\theta \end{bmatrix} g \tag{3}$$

$$\begin{bmatrix} \dot{p} \\ \dot{q} \\ \dot{r} \end{bmatrix} = [\vec{I}]^{-1} \begin{bmatrix} 0 & r & -q \\ -r & 0 & p \\ q & -p & 0 \end{bmatrix} [\vec{I}] \begin{bmatrix} p \\ q \\ r \end{bmatrix} + [\vec{I}]^{-1} \begin{bmatrix} M_L \\ M_M \\ M_N \end{bmatrix} \tag{4}$$

where m is the mass, $[\vec{I}]$ is the inertia tensor, and g is the gravitational acceleration. The $[F_X \quad F_Y \quad F_Z]^T$ and $[M_L \quad M_M \quad M_N]^T$ terms are the aerodynamic forces and moments, respectively.

The aerodynamic model provides the aerodynamic forces and moments at a given angle of attack and Mach number using aerodynamic coefficient data.[11,12]

$$F_X = -QS\left[C_{X_0}(M) + C_{X_{\bar{\alpha}^2}}(M)\sin^2\bar{\alpha}\right] \tag{5}$$

$$F_Y = -QS\left[C_{N_\alpha}(M)\sin\beta + C_{N_{\alpha^3}}(M)\sin^3\beta\right] \tag{6}$$

$$F_Z = -QS\left[C_{N_\alpha}(M)\sin\alpha + C_{N_{\alpha^3}}(M)\sin^3\alpha\right] \tag{7}$$

$$M_L = QSD\left[C_{l_\delta}(M)\delta_F + C_{l_p}(M)\frac{pD}{2V}\right] \tag{8}$$

$$M_M = QSD\left[C_{m_\alpha}(M)\sin\alpha + C_{m_{\alpha^3}}(M)\sin^3\alpha + C_{m_q}(M)\frac{qD}{2V}\right] \tag{9}$$

$$M_N = QSD\left[-C_{m_\alpha}(M)\sin\beta - C_{m_{\alpha^3}}(M)\sin^3\beta + C_{m_q}(M)\frac{rD}{2V}\right] \tag{10}$$

where α is the angle of attack, β is the angle of sideslip, $\bar{\alpha} = \sqrt{\alpha^2 + \beta^2}$ is the total angle of attack, δ_F is the fin cant, D is the projectile diameter, V is the projectile velocity, $Q = \frac{1}{2}\rho V^2$ is the dynamic pressure, and $S = \frac{\pi}{4}D^2$ is the aerodynamic reference area.

Aerodynamic data describing the forces and moments due to the wing are applied separately from the aerodynamic data for the Body-Fin-Canard (BFC) assembly. By modifying the wing-only aerodynamic data, the effect of changing the wing size and location on the flight behavior can be explored.

Equations 5–10 describe the Body-Fin (BF) and reflect the symmetry of that assembly. The aerodynamic model for the moveable control surfaces has a slightly different formulation in order to capture asymmetries and to include nonlinearities (see Eq. 13).

4. Aerodynamic Characterization

A comprehensive aerodynamic characterization of the body and aerodynamic lifting surfaces was performed using a combination of modeling and experimentation. SEAP is an effective initial aerodynamic characterization technique as it allows for rapid performance evaluation of airframes throughout all Mach regimes. A combination of two SEAP codes were used to help characterize the aerodynamics for all configurations: 1) Projectile, Rockets, and Ordnance Design and Analysis System (PRODAS) tool suite by Arrow Tech Associates[14] (i.e., SEAP Model 1) and 2) Missile DATCOM[15] (i.e., SEAP Model 2). The graphical user interface MissileLab[16] was employed to create input files and execute Missile DATCOM (Fig. 2). These engineering-level computer programs package together several ballistics methodologies, leveraging theoretical and empirical methods to encompass the entire speed regime from subsonic to supersonic flight, in order to estimate aerodynamic parameters of conventional munition configurations. In addition to static aerodynamic parameters, these SEAP methodologies include calculations of dynamic aerodynamics derivatives (e.g., roll damping moment, pitch damping moment), providing an adequate estimate for the complete aerodynamic database used in flight simulations.

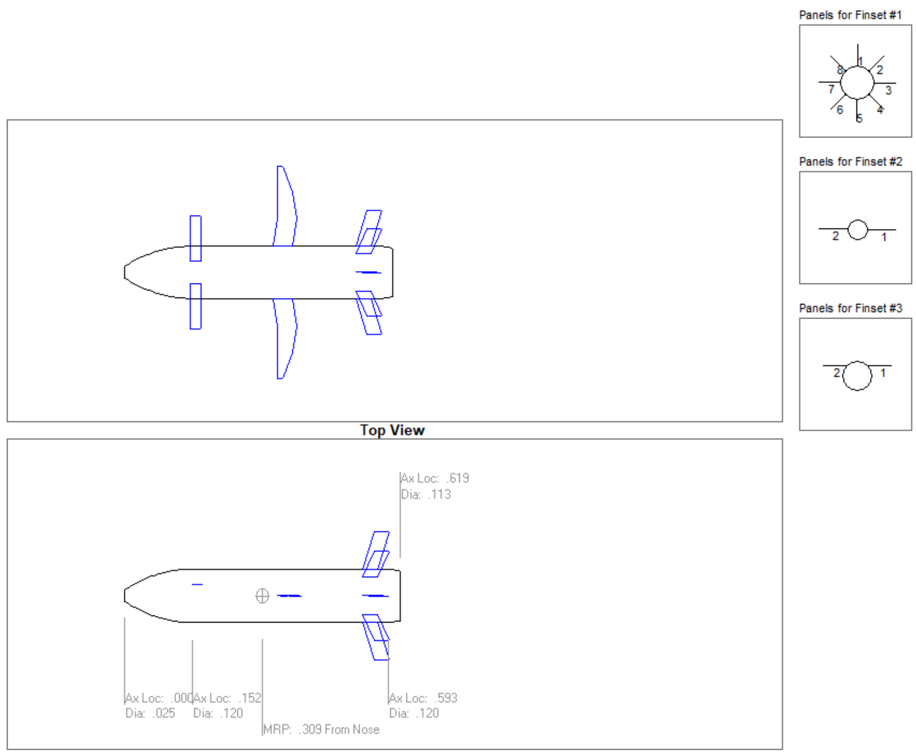

Fig. 2 Geometry sketch of projectile concept modeled in MissileLab and executed in Missile DATCOM

NASA's Cartesian Euler (CE) CFD analysis package, Cart3D,[17] uses the simplifying assumption of inviscid flow to quickly generate static aerodynamic coefficients of complex configurations while often providing better accuracy than SEAP. The Euler flow solver has proven valuable for many applications, including optimization and aircraft design analysis.[18–26]

The initial sizing of the stabilizing and control surfaces shown in Fig. 1 was determined through a combination of SEAP and CE CFD. SEAP was used to determine the number, location, and size of tail fins necessary to remain statically stable from launch to impact (Mach 2.7 and below).

Initial flight simulations using the aerodynamic coefficients generated through SEAP indicated a Mach number of approximately 0.5 during the glide phase of flight. Using CE CFD, the location of the canards and wing were varied parametrically to determine an optimal configuration that maximizes the lift-to-drag ratio of the projectile at Mach 0.5. The wing angle of attack was 0°, and the wing size was held constant for this initial analysis. In all cases, the canards were set to a constant +10° deflection in order to produce a positive, nonzero body trim angle. Various body angles of attack were analyzed for each configuration: $\alpha =$ 15°, –10°, –5°, –3°, 0°, 3°, 5°, 10°, and 15°. The canard deflection angle was limited to 10° in order to minimize the onset of flow separation and potential complex flow interactions. At larger deflection angles, both SEAP and CE CFD methods lose accuracy, making the aerodynamics more difficult to characterize.

The Cart3D analysis package automatically creates a Cartesian computational grid around the geometry after setting the domain’s extent and resolution. The process is able to automatically increase fidelity of the domain near small features and curvature of the geometry, therefore better resolving the flow features present near the surface. A typical generated computational domain is shown in Fig. 3. The computational domain extended to 50 diameters in all directions from the center of the body, and the smallest typical grid size for the domain was approximately 0.1 × 0.1 × 0.1 mm. The typical computational grid consisted of approximately 10 million Cartesian cells. The flow solver (flowCart) exploits the features of the Cartesian grid to quickly compute the static aerodynamic forces and moments experienced by the configuration.

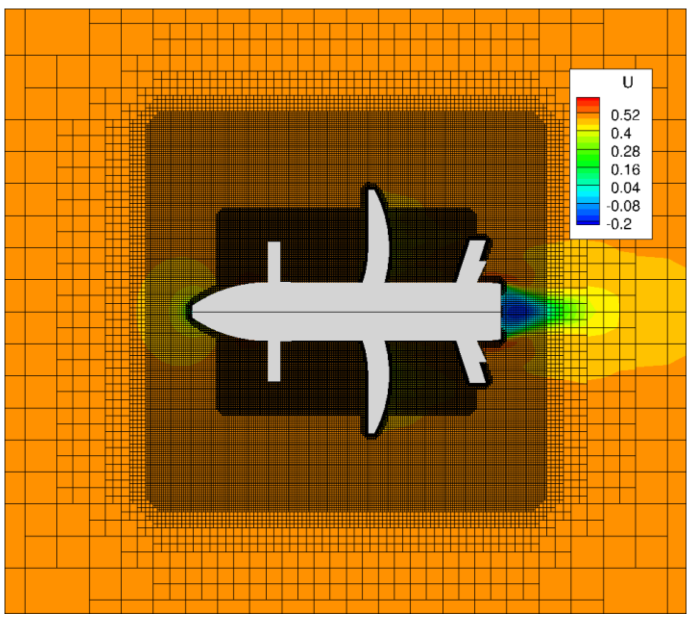

Fig. 3 Contour of simulated non-dimensional streamwise velocity superimposed with the computational domain (Cart3D)

The performance of each configuration was evaluated based on the lift-to-drag at the body trim angle for a +10° canard deflection, and the optimal configuration yielding the highest lift-to-drag ratio was identified. Once the optimal design shown in Fig. 1 was identified, the aerodynamic forces and moments were calculated across Mach 0.1–2.7 using both SEAP and CE CFD to characterize the aerodynamics throughout the flight envelope. This approach was developed and applied in Vasile et al.[27]

In order to validate and augment the SEAP and CE CFD aerodynamic characterization, static aerodynamic data were collected through wind tunnel experiments. Subsonic experiments at Mach 0.2 were conducted in a continuous flow, in-draft wind tunnel with a 0.71 m (28 inch) high by 1 m (40 inch) wide cross section and 1.52 m (60 inch) length, housed at the US Army Edgewood Chemical and Biological Center at Aberdeen Proving Ground, Maryland. Since aerodynamics do not vary appreciably with Mach in the subsonic regime, the WT experiments provide data necessary to more accurately simulate flight over the critical glide (subsonic) phase of flight.

The WT experimental model (Fig. 4) was designed to be modular, such that multiple combinations of body, and stabilizing and control surfaces could be evaluated separately (e.g., body alone, body and canards, body and canards and wings). The 60-mm-diameter model was constructed from selective laser sintered glass-filled nylon, and the control surfaces were cut from 1 mm thick spring steel sheet. The model was mounted on a sting with a 0.95 cm (3/8 inch) diameter, five component balance (Modern Machine and Tool Co.). The balance featured sensitivities of 44.5 N (10 lb) for axial force, 35.6 N (8 lb) for normal force, 22.2 N (5 lb) for side force, and 0.9 N-m (8 inch-lb) for pitching moment and side moment. The balance is accurate to ± 0.032 N (0.0072 lb). The blockage ratio for the model (i.e., projected area of projectile divided by the tunnel cross-sectional area) was calculated to be less than 1%, and therefore was assumed to be negligible. An image of the model with balance on the sting in the tunnel is shown in Fig. 4.

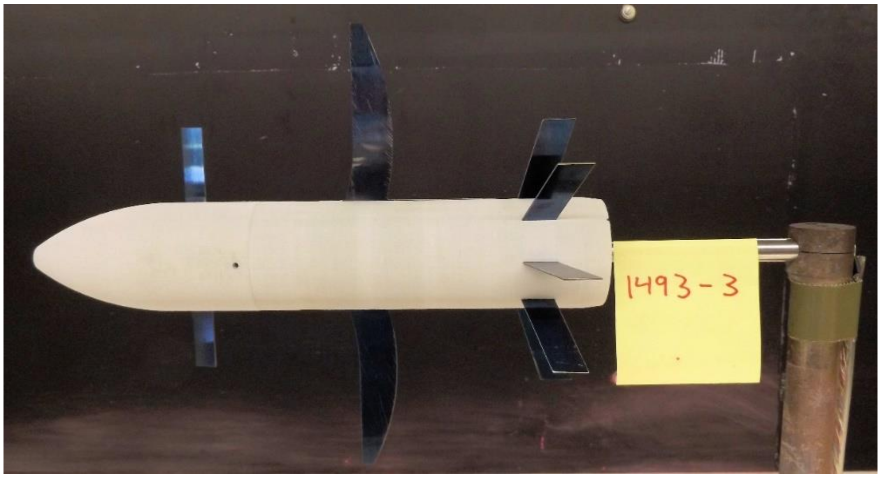

Fig. 4 Instrumented model mounted in WT facility test section

Data were obtained in the WT at total angles of attack of ±14° in 1° increments. The balance collected 1000 samples after steady-state flow conditions were met at each angle of attack. The averaged measured value was computed for each component. The wind tunnel data collected were least-squares fit with an appropriate polynomial expansion in angle of attack.

Aerodynamic characterizations were performed of the body and of the body with each stabilizing and control surface separately. To isolate the maneuver aerodynamics, a method of superposition was used; the body aerodynamic data were subtracted from the body with stabilizing and control surfaces data. Thus, both wing and canard and any control surface interference effects were modeled as part of the maneuver aerodynamics.

The aerodynamic characterization was formulated by incorporating all aerodynamic techniques (i.e., SEAP models, CE CFD, and WT). Subject matter expertise was applied to reconcile the best aerodynamic data available from the various sources into one cohesive data set while minimizing discontinuities and ensuring smoothness across Mach number for each of the aerodynamic parameters. This blended aerodynamic data is used as the data set for the munition in subsequent flight dynamic analyses.

Some examples of aerodynamic data and subsequent polynomial models are shown in Fig. 5. In these plots, the WT data is represented by open markers, while the dashed curves represent the polynomial fit to the data. The results from the CE CFD solution at Mach 0.2 is presented using solid symbols, with polynomial fit of the data depicted by dashed curves. The SEAP results are depicted by dashed curves. The resulting blended aerodynamic data at Mach 0.2 is shown as solid lines. Three configurations are presented; the Body only (B), the Body-Fin (BF), and the Body-Fin-Wing-Canard (BFWC) at 0° canard deflection (Figs. 5a–b, c–d, e–f respectively). The blended aerodynamic data uses the SEAP Model 2, CE CFD, and WT sources to capture higher order terms in the aerodynamic model representative of complex flows, therefore improving the accuracy of the aerodynamics at higher angles of attack. As expected, the magnitudes of normal force coefficient and pitching moment coefficient increase with the addition of control surfaces. The normal force coefficient (Figs. 5b, d, f) from CE CFD compares well to the experimental data at small angles of attack. At higher angles of attack, the CE CFD flow solver is unable to accurately predict flow separation, therefore overpredicting the normal force at angles of attack greater than 7°. The vortex models in SEAP Model 2 provide a more accurate prediction of vortex-fin interference effects. Similarly, the pitching moment coefficients from all sources compare relatively well to WT. The differences could be attributed to a laminar-toturbulent transition on the wind tunnel model that is not included in the inviscid simulations, which ultimately would affect the location of the center of pressure.

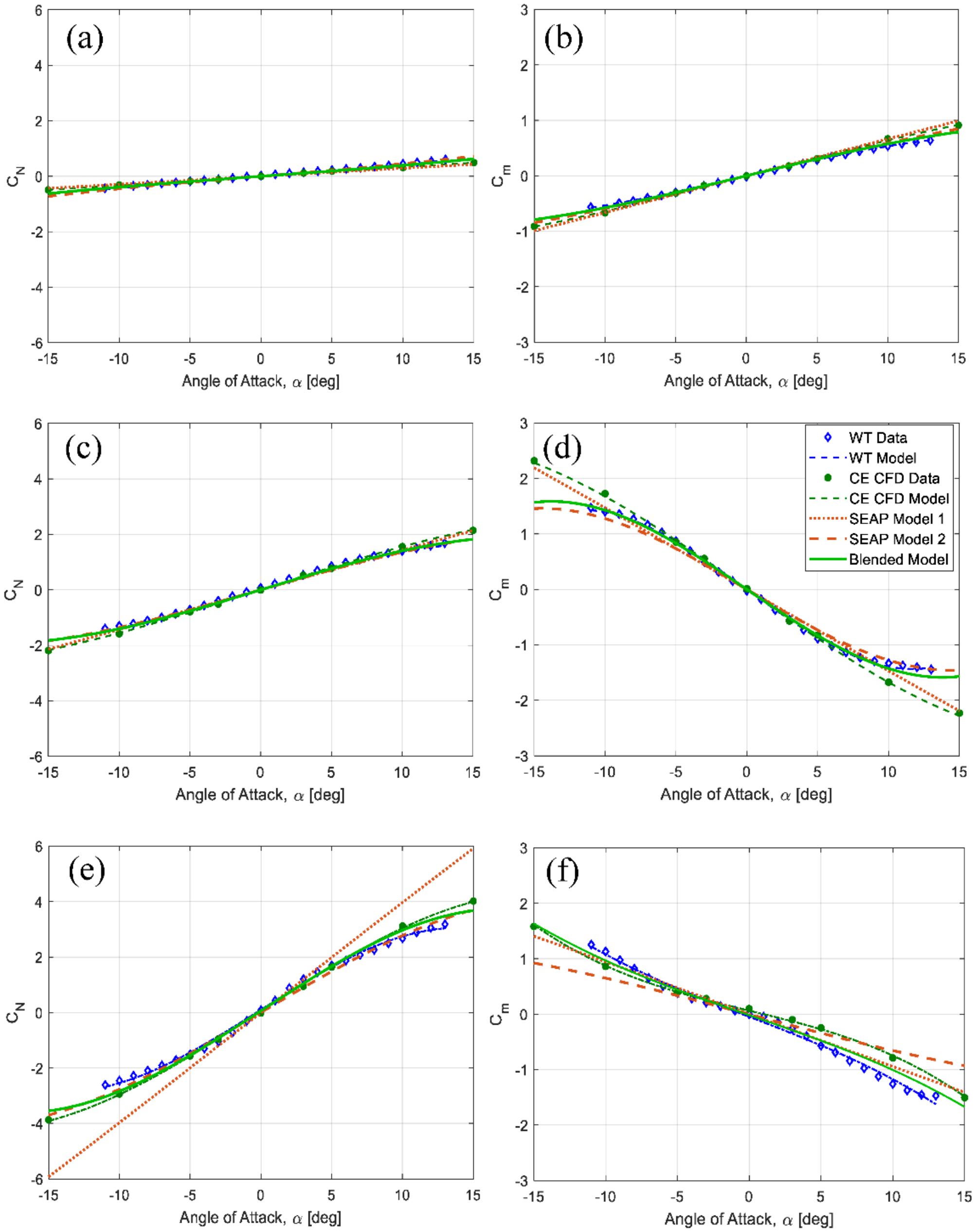

Fig. 5 Normal force coefficient (a, c, e) and pitching moment coefficient (b, d, f) of B (a–b), BF (c–d), and BFWC (e–f) configurations at Mach 0.2 from WT only, CE CFD only, SEAP only, and blended (SEAP, CE CFD, and WT) data

Since the WT data were collected at Mach 0.2, the computed subsonic aerodynamic coefficients from the blended aerodynamic model were corrected based on the difference between the data at Mach 0.2. This correction was then applied across all Mach numbers below 1.0, with a linear transition back to the uncorrected SEAP Model 2 data (i.e., DATCOM) at Mach numbers greater than 1.0. Between the SEAP models studied, it was evident that the SEAP Model 2 data compared best to both CE CFD and WT data.

The lowest relevant order of the polynomial expansions for the aerodynamic coefficients from all sources and the blended aerodynamic data at multiple Mach numbers are presented in Figs. 6 and 7. The BFWC aerodynamic data were only computed for Mach numbers below 1 since the flight regime the vehicle experiences during glide out is subsonic (i.e., canards deploy at apogee and glide at subsonic speeds until terminal impact). The zeroth-order coefficient of axial force for B, BF, and BFWC at 0° canard deflection is presented in Figs. 6a, b, and c, respectively. For all configurations, as Mach number approaches 1, the magnitude of the aerodynamic coefficients increase until reaching a maximum at Mach 1. Furthermore, the additional control surfaces increase the axial force. Overall, the results from the CE CFD and SEAP models compare and agree well with the WT data. The axial force computed by the CE CFD is expected to be low since the inviscid flow assumption neglects the skin friction component. In addition, the inviscid solver can be a poor predictor of flow separation unless there is a sharp discontinuity in flow direction (e.g., wake flow, fin/canard at higher angle of attack).

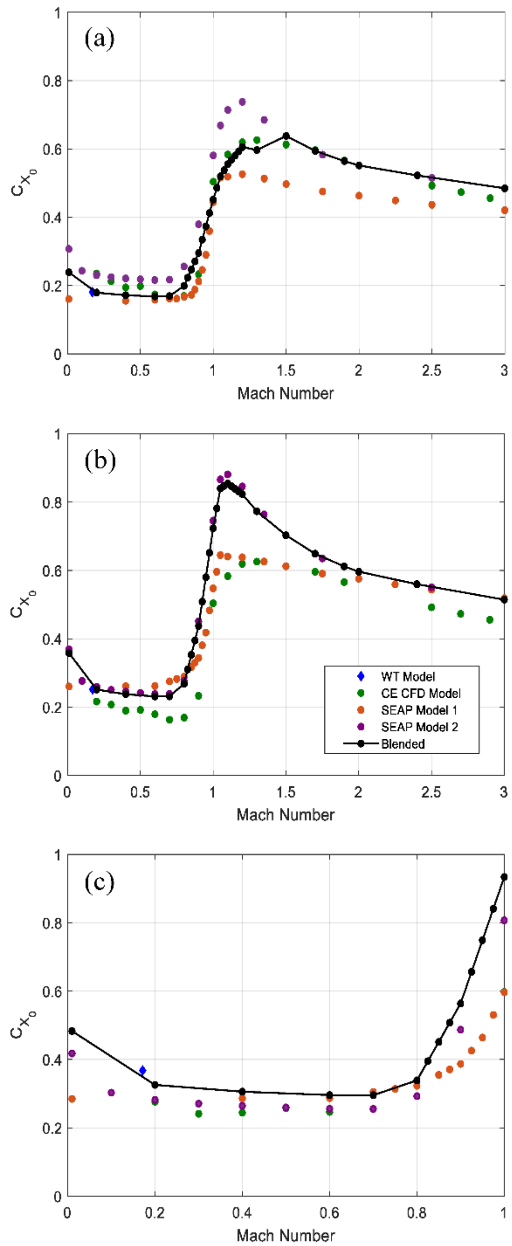

Fig. 6 Zeroth-order coefficient of axial force for B (a), BF (b), and BFWC (c) configurations from SEAP, CE CFD, WT only, and blended (SEAP, CE CFD, and WT) data across Mach number.

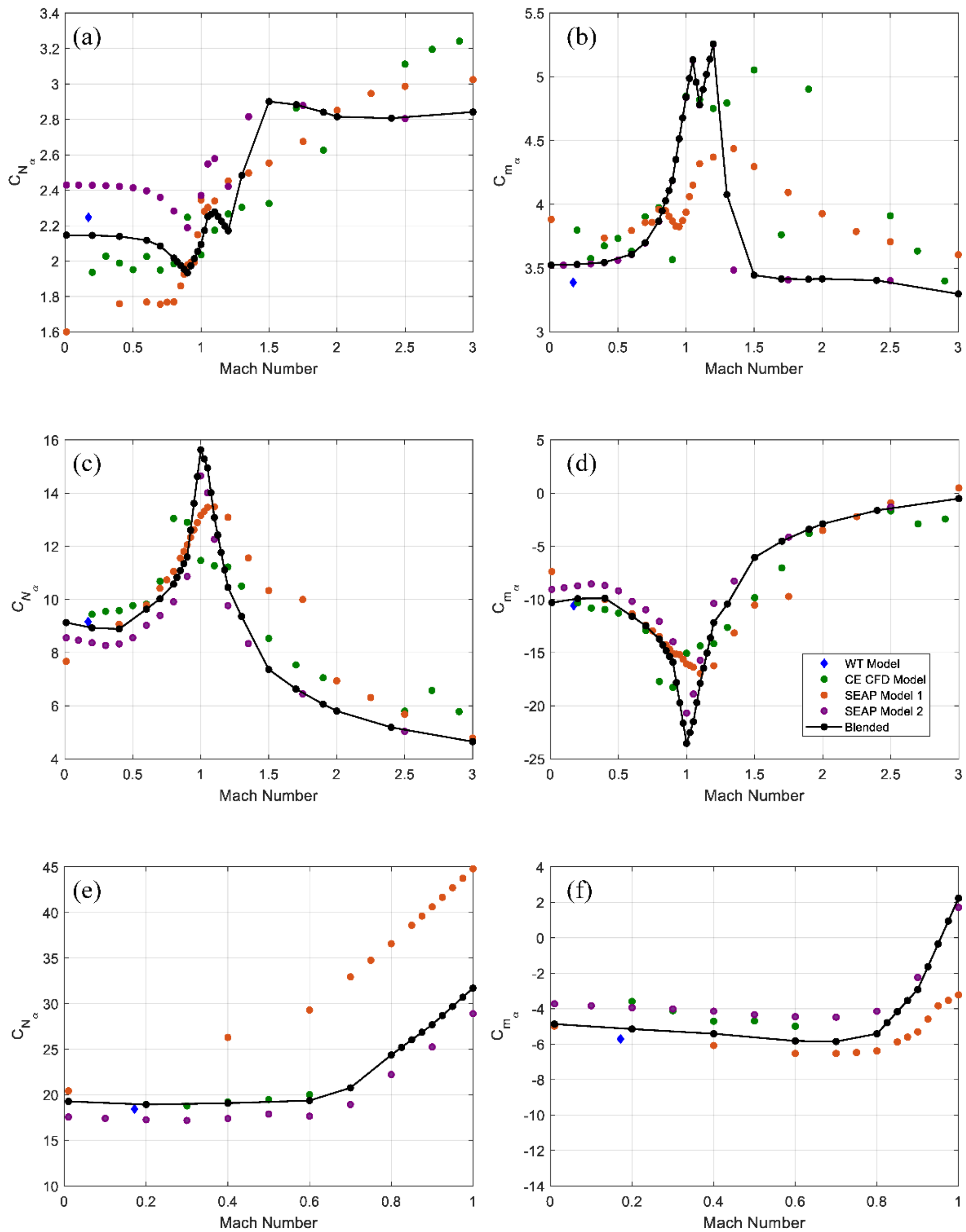

Fig. 7 First-order coefficient of static normal force and static pitching moment for BF and BFWC configurations from SEAP, CE CFD, WT only, and blended (SEAP, CE CFD, and WT) data across Mach number

The first-order coefficients for normal force coefficient and pitching moment coefficient for B, BF, and BFWC at 0° canard deflection are presented in Figs. 7a, c, and d and Figs. 7b, d, and e, respectively. Overall, the data sources compare well, and the blended aerodynamic data reconciles the sources to produce a smooth cohesive data set that captures the nonlinear behavior as predicted from SEAP, CE CFD, and WT.

Tables 2 and 3 present the polynomial expansions describing the final blended aerodynamic data set for B and BF, while the final blended aerodynamic coefficients of the baseline wing and canard surfaces alone are presented in Tables 4 and 5, respectively. All aerodynamic data sets contain second-order polynomial fit coefficients for the axial force, and third-order fit coefficients for normal force and pitching moment across Mach number. These higher-order terms are used to capture the nonlinear effects such as flow separation that limit flight performance, however these effects are difficult to assess and additional modeling and experimentation is required to develop a more complete aerodynamic characterization at high angles of attack.

Table 2 Aerodynamic data set for B

Mach	C_{X_0}	$C_{X_{\bar{\alpha}^2}}$	C_{N_α}	$C_{N_{\alpha^3}}$
0.01	0.2388	2.1114	9.1323	–28.8730
0.2	0.1811	1.3509	8.9378	–28.4992
0.4	0.1717	1.2376	8.8984	–27.3437
0.6	0.1683	1.2063	9.6345	–29.0798
0.7	0.1702	1.1880	10.0323	–29.4830
0.8	0.2017	0.4639	10.5959	–28.9674
0.825	0.2231	0.4961	10.8328	–29.1594
0.85	0.2471	0.5709	11.0878	–29.4149
0.875	0.2711	0.6465	11.3431	–29.6717
0.9	0.2997	0.7323	11.8250	–30.2115
0.925	0.3342	0.8316	12.6072	–31.1264
0.95	0.3734	0.9411	13.6160	–32.3244
0.975	0.4125	1.0505	14.6247	–33.5224
1	0.4506	1.1565	15.3530	–33.9222
1.025	0.4857	1.2528	15.2925	–32.0774
1.05	0.5150	1.3353	14.7756	–28.7363
1.075	0.5375	1.4039	14.0181	–24.4399
1.1	0.5546	1.4473	13.1121	–19.6502
1.125	0.5676	1.3684	12.4296	–16.5333
1.15	0.5802	1.2771	11.7696	–13.5844
1.175	0.5927	1.1846	11.1120	–10.6539
1.2	0.6010	1.0743	10.5662	–8.0943
1.3	0.5985	0.4720	9.3699	–1.1684
1.5	0.6350	–0.8964	7.4085	10.0991
1.7	0.5940	–0.8504	6.6327	15.7825
1.9	0.5642	–0.7791	6.0629	20.1982
2	0.5516	–0.7469	5.8059	22.1972
2.4	0.5223	–0.5670	5.1918	24.0080
3	0.4846	–0.2873	4.6498	22.3293

Table 3 Aerodynamic data set for BF

Mach	C_{X_0}	$C_{X_{\bar{\alpha}^2}}$	C_{N_α}	$C_{N_{\alpha^3}}$	C_{m_α}	$C_{m_{\alpha^3}}$	C_{l_δ}	C_{m_q}	C_{l_p}
0.01	0.3584	1.6795	9.1323	–28.8730	–10.3007	57.8246	0.0000	–187.8591	–8.9819
0.2	0.2547	1.0744	8.9378	–28.4992	–9.9345	58.4725	0.0000	–186.9906	–8.7969
0.4	0.2380	0.9847	8.8984	–27.3437	–9.9074	57.7913	0.0000	–195.5859	–8.9420
0.6	0.2317	0.9594	9.6345	–29.0798	–11.5900	62.0356	0.0000	–227.7294	–10.1021
0.7	0.2332	0.9459	10.0323	–29.4830	–12.4942	63.3737	0.0000	–247.6659	–10.9632
0.8	0.2737	0.3684	10.5959	–28.9674	–13.7680	63.6234	0.0000	–276.9004	–12.0365
0.825	0.3108	0.3942	10.8328	–29.1594	–14.2746	64.3062	0.0000	–287.1705	–12.4807
0.85	0.3530	0.4539	11.0878	–29.4149	–14.8166	65.1106	0.0000	–297.9925	–12.9584
0.875	0.3953	0.5143	11.3431	–29.6717	–15.3594	65.9174	0.0000	–308.8248	–13.4367
0.9	0.4464	0.5826	11.8250	–30.2115	–16.3133	67.5477	0.0000	–325.2075	–14.2339
0.925	0.5090	0.6614	12.6072	–31.1264	–17.8118	70.2689	0.0000	–348.9413	–15.4536
0.95	0.5803	0.7481	13.6160	–32.3244	–19.7216	73.8137	0.0000	–378.2254	–16.9923
0.975	0.6517	0.8348	14.6247	–33.5224	–21.6313	77.3585	0.0000	–407.5095	–18.5309
1	0.7204	0.9189	15.3530	–33.9222	–22.9324	79.9035	0.0000	–430.4095	–19.7728
1.025	0.7817	0.9956	15.2925	–32.0774	–22.5217	79.6366	0.0000	–435.3561	–20.1804
1.05	0.8250	1.0617	14.7756	–28.7363	–21.2691	76.7788	0.0000	–428.9360	–19.8696
1.075	0.8473	1.1168	14.0181	–24.4399	–19.6972	71.7439	0.0000	–415.6981	–18.9818
1.1	0.8528	1.1512	13.1121	–19.6502	–17.9295	65.2347	0.0000	–398.1020	–17.7150
1.125	0.8465	1.0824	12.4296	–16.5333	–16.4673	59.6785	0.0000	–385.6049	–16.7973
1.15	0.8389	1.0033	11.7696	–13.5844	–15.0357	54.2180	0.0000	–373.6197	–15.9146
1.175	0.8312	0.9231	11.1120	–10.6539	–13.6076	48.7680	0.0000	–361.6907	–15.0358
1.2	0.8221	0.8252	10.5662	–8.0943	–12.4663	44.0920	0.0000	–350.8561	–14.2697
1.3	0.7743	0.2757	9.3699	–1.1684	–10.3937	32.2689	0.0000	–317.7816	–12.2267
1.5	0.7037	–0.9031	7.4085	10.0991	–6.1409	13.1103	0.0000	–273.8673	–9.3287
1.7	0.6491	–0.8503	6.6327	15.7825	–4.5239	6.5587	0.0000	–253.9345	–8.0702
1.9	0.6123	–0.7790	6.0629	20.1982	–3.3949	1.7478	0.0000	–237.9313	–7.2158
2	0.5966	–0.7469	5.8059	22.1972	–2.8951	–0.4180	0.0000	–230.4382	–6.8429
2.4	0.5600	–0.5669	5.1918	24.0080	–1.6244	–3.2572	0.0000	–205.9326	–5.6185
3	0.5145	–0.2872	4.6498	22.3293	–0.5069	–4.4214	0.0000	–177.8484	–4.4426

Table 4 Aerodynamic data set for wing surface only

Mach	C_{X_0}	$C_{X_{\bar{\alpha}^2}}$	C_{N_α}	$C_{N_{\alpha^3}}$	C_{m_α}	$C_{m_{\alpha^3}}$
0.01	0.0847	0.3582	8.1835	–48.0392	–0.1887	–31.6830
0.2	0.0518	0.2290	8.0521	–40.9467	–0.5084	–29.4571
0.4	0.0466	0.2098	8.2141	–35.6277	–0.7791	–27.3371
0.6	0.0445	0.2075	8.4982	–30.3871	–0.1949	–31.4178
0.7	0.0442	0.2029	8.6423	–25.2681	–0.4070	–33.0625
0.8	0.0496	0.0801	11.7111	–25.4544	–0.1284	–41.1982
0.825	0.0566	0.0858	12.3321	–24.1476	0.1103	–44.1159
0.85	0.0647	0.0987	12.9189	–22.5688	0.3805	–47.1903

Table 4 Aerodynamic data set for wing surface only (continued)

Mach	C_{X_0}	$C_{X_{\bar{\alpha}^2}}$	C_{N_α}	$C_{N_{\alpha^3}}$	C_{m_α}	$C_{m_{\alpha^3}}$
0.875	0.0727	0.1117	13.5050	–20.9850	0.6513	–50.2676
0.9	0.0824	0.1264	13.9659	–18.3595	1.2215	–54.6481
0.925	0.0941	0.1432	14.2609	–14.3543	2.1883	–60.7545
0.95	0.1073	0.1617	14.4306	–9.3076	3.4547	–68.1641
0.975	0.1206	0.1801	14.6003	–4.2608	4.7210	–75.5737
1	0.1323	0.1980	14.7895	–0.2474	5.4797	–80.6206

Table 5 Aerodynamic data set for single canard blade

Mach	C_{X_0}	$C_{X_{\bar{\alpha}^2}}$	C_{N_α}	$C_{N_{\alpha^3}}$	C_{m_α}	$C_{m_{\alpha^3}}$	C_{l_α}
0.01	0.0201	0.0794	0.9792	–2.5906	2.8114	–9.9161	0.7052
0.2	0.0119	0.0504	0.9791	–2.1154	2.6477	–25.7814	0.8658
0.4	0.0106	0.0461	0.9846	–1.3149	2.6374	–35.2888	1.0348
0.6	0.0101	0.0449	0.6628	1.4134	2.9890	–37.4935	1.2036
0.7	0.0100	0.0433	1.0878	0.4759	3.5340	–29.9029	1.3590
0.8	0.0114	0.0176	1.0267	2.0359	4.2825	–2.4975	1.5149
0.825	0.0139	0.0185	1.0184	2.7458	4.6881	7.5979	1.5772
0.85	0.0168	0.0210	1.0125	3.5117	5.1355	18.2790	1.6396
0.875	0.0198	0.0234	1.0067	4.2787	5.5837	28.9709	1.7018
0.9	0.0230	0.0264	0.9765	5.1077	6.1877	41.8088	1.7644
0.925	0.0267	0.0301	0.9139	6.0187	6.9981	57.4887	1.8257
0.95	0.0307	0.0343	0.8269	6.9918	7.9644	75.3146	1.8874
0.975	0.0347	0.0384	0.7399	7.9648	8.9307	93.1404	1.9490
1	0.0379	0.0425	0.6477	8.8537	9.6063	105.0992	2.0109

5. Aerodynamic Analysis of Wing

5.1 Wing Effect on Lift-to-Drag Ratio

Range is dependent on the glide slope; an airframe with a higher lift-to-drag ratio is able to more efficiently trade altitude for range as it descends. Figure 8 plots the lift-to-drag ratio across angle of attack for the BFC configuration with no wing, and for the BFWC with several different wing sizes. The wing-only lift-to-drag ratio is included for reference; as the proportion of the total aerodynamics due to the wing increases, the lift-to-drag trends toward the wing-only performance curve. These results assume the canards are deflected to 5°, and the velocity for these results is Mach 0.5. The trends are representative of all subsonic velocities.

Overall, the addition of a wing increases the projectile lift-to-drag, with larger wings providing a larger increase at positive angles of attack. However, the rate of improvement in performance gains of the total configuration due to larger wings slows as wing size increases.

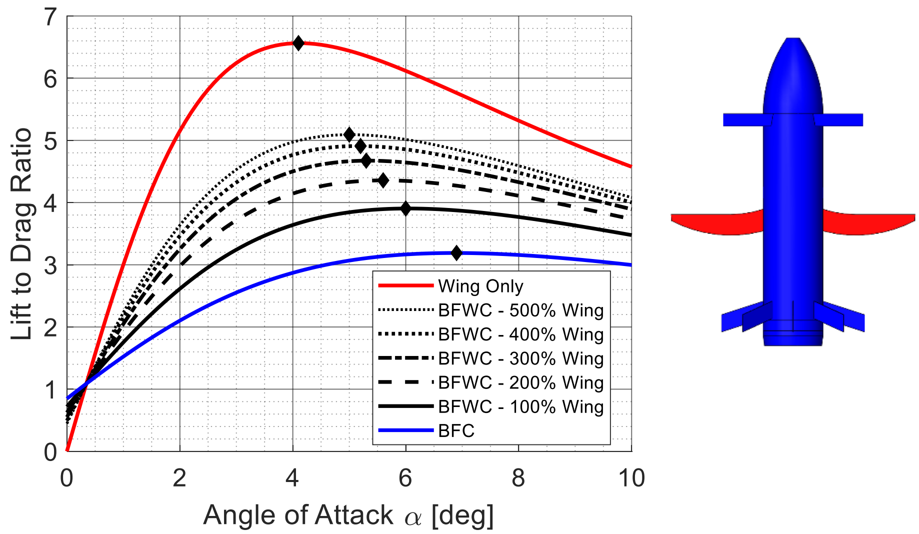

Fig. 8 Lift-to-drag ratio for the BFC, the wing alone, and the BFWC for several wing sizes at Mach 0.5. The optimal angles of attack corresponding to the highest lift-to-drag ratios for each configuration are marked with diamonds.

As illustrated in Fig. 8, the lift-to-drag is a function of the angle of attack, and each configuration has a peak lift-to-drag value that occurs at some optimal angle of attack. In this case, the optimal angle of attack is 6.9° for the BFC configuration and decreases to 6.0° for the nominal (100%) wing configuration. The optimal angle of attack continues to decrease to 5.0° as the wing size increases to 500% of the nominal value.

The flight stability and the pitching moment provided by the deflected canards both influence the steady-state trim angle of attack of the body. A configuration with large static stability featuring small aerodynamic control surfaces may not be able to achieve a steady-state pitch maneuver at the optimal angle of attack to attain the maximum lift-to-drag ratio. This situation results in a trim condition at a smaller angle of attack corresponding to a sub-optimal lift-to-drag ratio.

This research is focused on the wing characteristics, so the canard size and location are held constant for this analysis. However, the wing impacts the stability of the overall configuration, and therefore influences the steady-state trim angle of the body. Depending on the specifics of the airframe, the overall static stability can be decreased by adjusting the location of a given wing planform, enabling the pitching moment imparted by the deflected canards to achieve the optimal trim angle to maximize the lift-to-drag.

5.2 Wing Effect on Static Margin

The static margin is a metric describing the static stability of a flight body, and is defined as the distance between the location of the center of gravity (CG) and the aerodynamic center of pressure (CP) as shown in Eq. 11:

$$Static\ Margin = CP - CG, \tag{11}$$

with the CG and CP locations measured from the projectile nose, positive static margin corresponds to stability, while negative static margin indicates instability.

The static margin at different angles of attack for both the BF and BFWC configurations are presented in Fig. 9. The BF configuration is statically stable throughout the subsonic region, and is stable for supersonic speeds up through the launch velocity of Mach 3. The BFWC configuration is marginally stable throughout the subsonic regime, which is the expected operating condition during the glide phase of flight when the control surfaces are deployed.

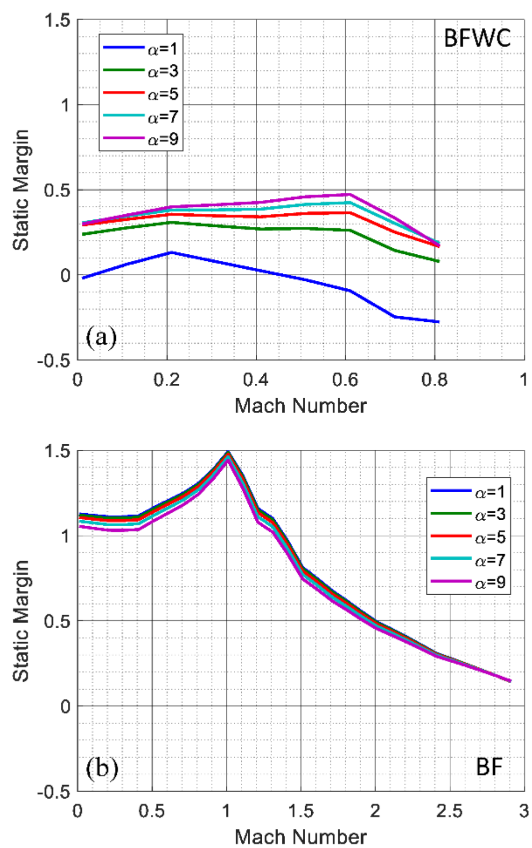

Fig. 9 Static margin of BF and BFWC configurations for varying α

Figure 10 shows the static margin in calibers across Mach for the BFC as well as for the contribution from the wing alone. The static margin for the BFWC is shown for increasing wing effectiveness, with BFWC stability decreasing as wing effectiveness increases.

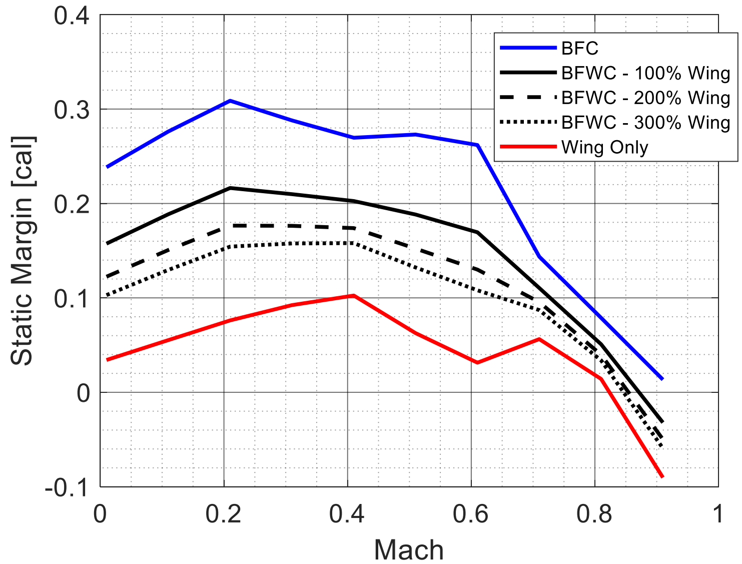

Fig. 10 Static margin at α=3° across Mach for the BFC, for the wing alone, and for the BFWC. Increasing the wing effect decreases the stability.

5.3 Effect of Wing Center of Pressure on Static Margin

Modifying the CP of the wing aerodynamic data enables an investigation into the effect of moving the wing along the projectile longitudinal axis, without changing the CG location. The effect on static margin due to adjusting the wing CP from the nominal design is shown in Fig. 11, which indicates shifting the wing CP toward the nose shifts the wing contribution to be more destabilizing.

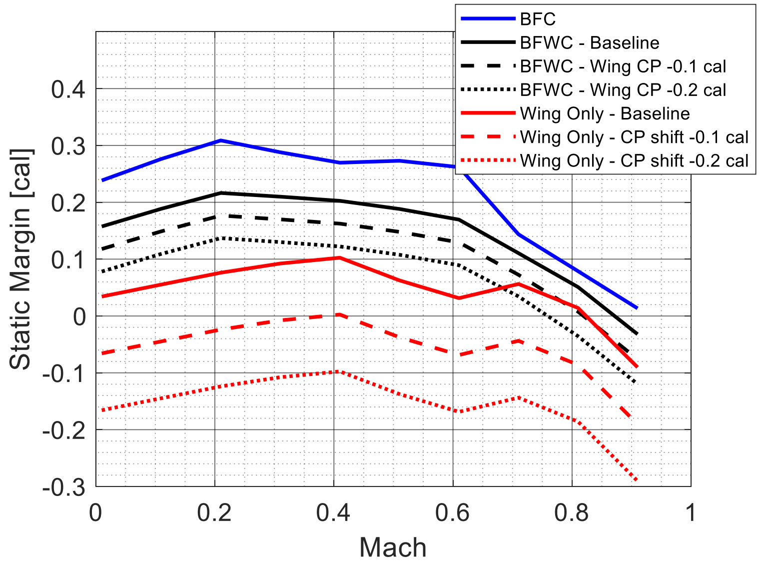

Fig. 11 Effect of shifting wing CP on wing static margin and static margin of BFWC. Shifting the wing CP toward the nose decreases the total stability.

5.4 Effect of Wing on Trim Angle

The steady-state trim angle of attack can be obtained by analyzing the static pitching moment as a function of attack angle and identifying the angle corresponding to zero moment (equilibrium). Using the nominal wing scaling and location, the pitching moment of the Body-Fin-Wing (BFW) configuration is shown in Fig. 12. The isolated contribution of the canards deflected at +5° is shown, along with the pitching moment of the BFWC. The combination of the body attack angle and the canard deflection angles results in stall and reduced lift beyond 5° canard deflection, so +5° is used throughout this analysis. The steady-state trim angle of the BFWC is found to be 3.5°, which is below the 6.0° optimal angle of attack needed to maximize the lift-to-drag for the nominal wing design shown in Fig. 8.

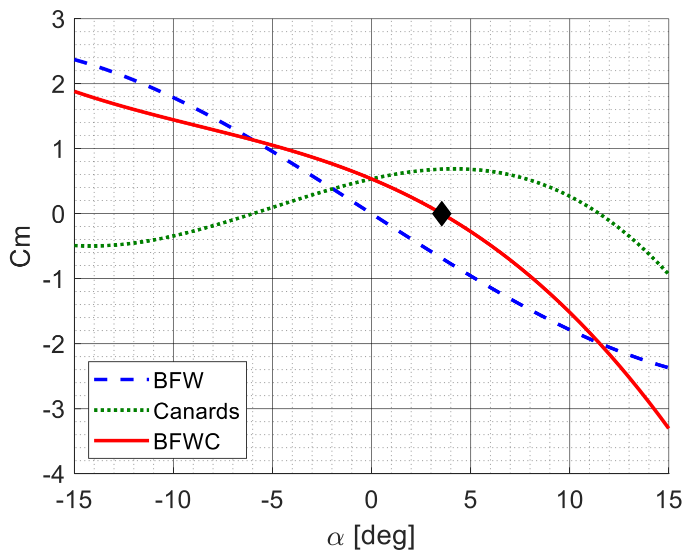

Fig. 12 Static pitching moment contributions from the BFW, from canards alone with +5° deflection, and the combined BFWC for Mach 0.5. The steady-state trim angle of attack of 3.5° is found where the total static pitching moment is zero, as indicated with a diamond.

As discussed in Section 5.3, shifting the wing CP forward has a destabilizing effect on the projectile, enabling the canard pitching moment to have a greater effect on the total projectile trim angle. Figure 13 shows the effect of changing the CP for the nominally sized wing on the BFWC static pitching moment with a constant +5° canard deflection. The less stable airframe configurations with forward shifted wings achieve a greater trim angle of attack under the same canard moment.

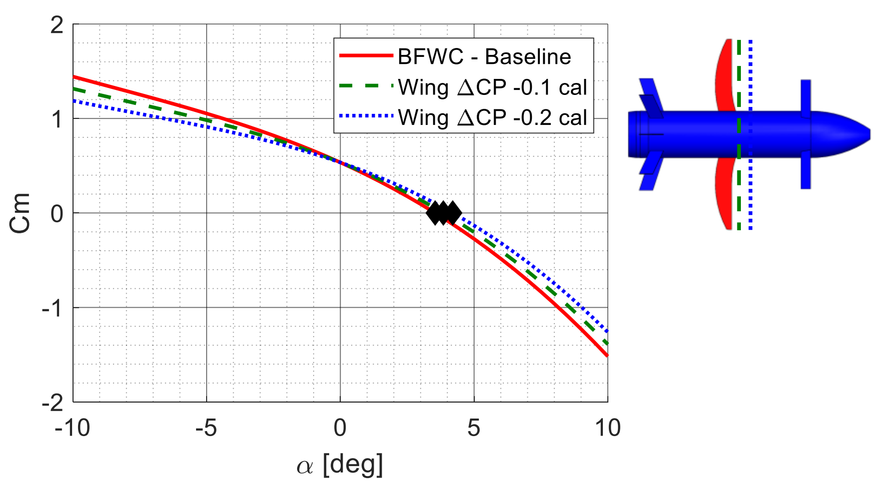

Fig. 13 BFWC static pitching moment at Mach 0.5 for nominally sized wings acting on the body at different CPs, with +5° canard deflection. Steady state trim angles of attack of 3.5°, 3.9°, and 4.2° are indicated with diamonds.

5.5 Optimized Wing Size and Location

The trim angle analysis presented in Section 5.4 suggests that for a particular wing size, an appropriate wing CP can be found to destabilize the configuration to the point where the moment created by the constant +5° canard deflection causes the trim angle to reach the optimal angle of attack, maximizing lift-to-drag for that particular wing size. An optimization analysis was performed for wings sized from 0% to 400%, across a set of ΔCPs ranging from +1 to –1 caliber. For each wing size and location, the trim angle was calculated, along with the corresponding lift-to-drag ratio. This lift-to-drag ratio is plotted as a function of wing size and CP in Fig. 14. The highest lift-to-drag for each wing size is achieved at a ΔCP that causes the airframe to be only marginally stable, enabling the canard moment to be more effective. The wing size and location parameters from several optimized designs are provided in Table 6, with the corresponding lift-to-drag ratio listed.

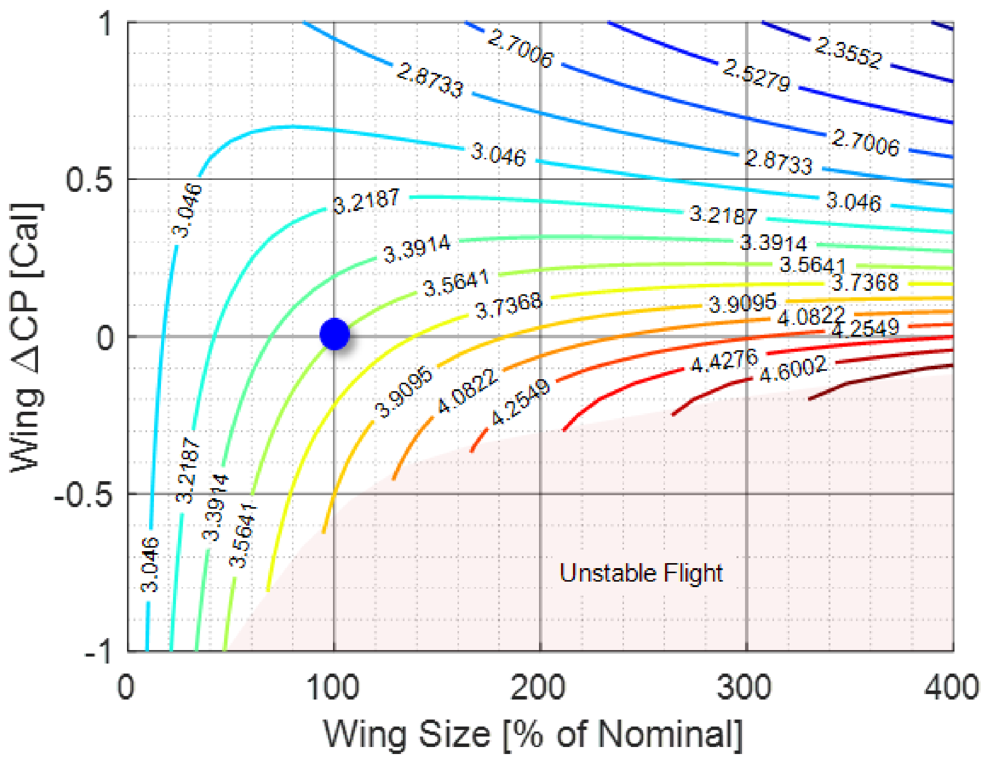

Fig. 14 Lift-to-drag ratio at steady-state trim angle of attack, plotted as a function of wing size and center of pressure at Mach 0.5. The nominal wing design is shown with a blue dot.

Table 6 Optimal wing designs

Wing size (% nominal)	Wing location (ΔCP) (caliber)	Trim angle (°)	Lift-to-drag at trim
0 (no wing)	NA	3.7	2.8
50%	–1	5.8	3.6
100%	–0.51	5.9	3.9
200%	–0.28	5.4	4.4
300%	–0.22	5.4	4.7
400%	–0.16	5.0	4.9

6. Flight Simulation

Trajectories were simulated using the wing sizing and location parameters listed in Table 6, with a 6 degrees-of-freedom flight model containing the flight dynamics and aerodynamics described in Section 3. An analysis was conducted of the relationship between the launch angle, wing and canard deployment time, and the munition range for each configuration listed in Table 6. For all cases in the analysis, the launch velocity was held fixed at 900 m/s (representative of legacy indirect fire weapons). The fins are deployed at launch, while the wing and canard remain stowed initially. A parametric analysis of the wing and canard deployment time indicates apogee deployment yields the best range for the munition at a given launch angle. Figure 15 shows the range of each configuration as a function of launch angle, and highlights the optimal launch angle for each. Each trajectory simulates an apogee wing and canard deployment with a +5° deflection added to the canards to pitch the body up for the remainder of flight.

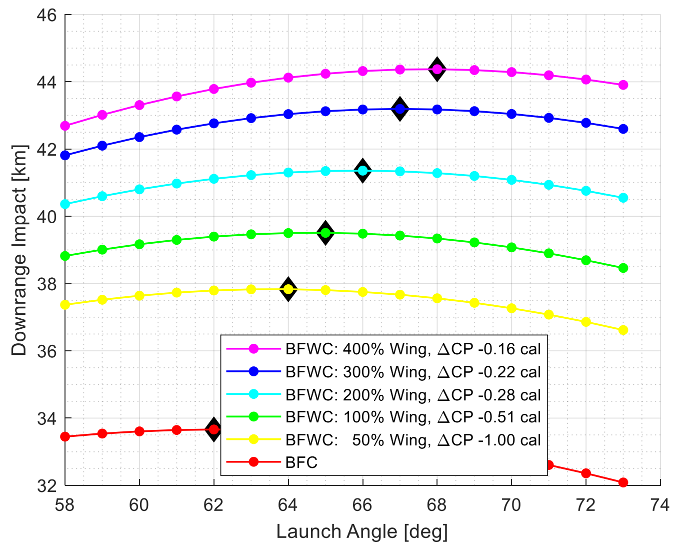

Fig. 15 Range as a function of launch angle for several configurations. Optimal launch angles for each are highlighted with a diamond.

The optimal launch angles for configurations with different wing designs are listed in Table 7, along with the maximum range. Figure 16 plots the trajectories for the wings described in Table 7, as well as for the ballistic BF configuration. Contrasting to the ballistic trajectory with an optimal launch angle near 45°, the best ranges for the gliding munitions result from steeper launch angles to loft the munition to higher altitude. This loft-to-glide trajectory enables the munition to begin its glide path from a higher altitude and maximize the benefit of a high lift-to-drag ratio.

Table 7 Best range of optimized munition configurations

Wing size (% nominal)	Wing location (ΔCP) (caliber)	Launch angle (°)	Range (km)	Range improvement (% over BFC glide)	Range improvement (% over BF ballistic)
no wing (BFC)	NA	62	33.6	…	132%
50%	–1	64	37.8	12.5%	161%
100%	–0.51	65	39.5	17.5%	172%
200%	–0.28	66	41.4	23.2%	186%
300%	–0.22	67	43.2	28.6%	198%
400%	–0.16	68	44.4	32.1%	206%

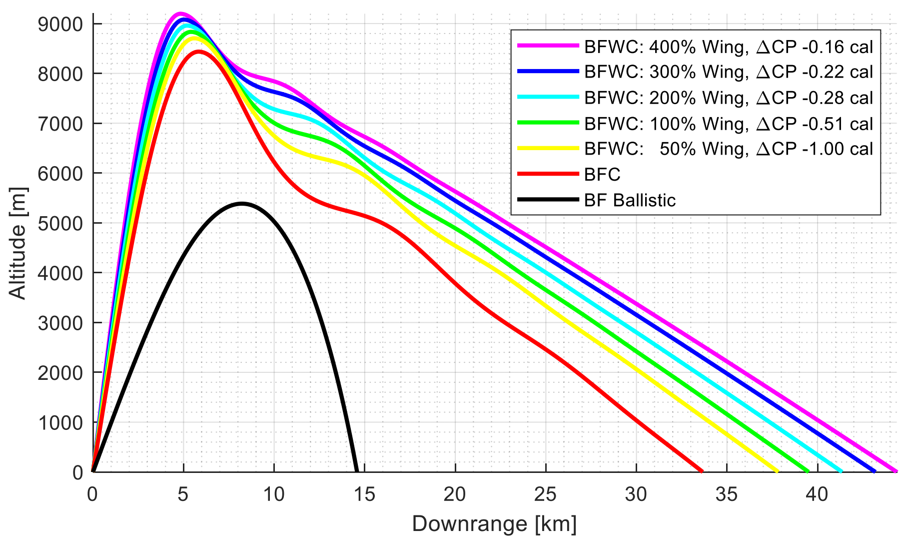

Fig. 16 Trajectories for configurations with the optimized wing designs described in Table 7

The flight simulations show the ballistic BF reaches 14.5 km, while the BFC glide achieves a range of 33.6 km by using the lift generated mainly by the body. The addition of the nominal sized wing (100%) with a CP shifted –0.51 calibers from the nominal location extends the range to 39.5 km, which is a 17.5% improvement over the BFC. Adding a wing with effects scaled to 200% of nominal, at a ΔCP of –0.28 calibers, improves the range to 41.4 km, for a 23.2% improvement over BFC.

As larger wings are added, the range continues to improve to 44.4 km for the 400% wing with a CP shifted –0.16 calibers from the nominal location, but the rate of improvement slows as wing size increases.

7. Conclusion

A framework was presented for understanding the range extension of gliding indirect-fire munitions equipped with enhanced lifting surfaces. This approach was demonstrated on a gun-launched artillery munition with wings. The munition concept was described and the flight dynamic and aerodynamic models were summarized. The aerodynamic characterization of the munition was provided in detail, incorporating contributions from semi-empirical aerodynamic prediction, inviscid flow CFD, and wind tunnel experiments. This aerodynamic characterization was then used in analytical and numerical tools to define the relationship between aerodynamic characteristics of the munition and the maximum glide range. This report outlines a general approach that can be applied to specific system constraints such as launch conditions (e.g., initial velocity and angle), munition size/weight, and subsystem allocation (e.g., warhead volume).

This study identified three critical aspects that must be combined to understand range extension of indirect fire munitions: 1) accurate aerodynamic characterization, 2) analytical vehicle optimization tools, and 3) high-fidelity flight simulation. Accurate aerodynamic characterization, including nonlinearities with angle of attack and deflection angle that result from complex flows such as separation and vortex interaction, drive the performance metrics (range, lift-to-drag) which dictate the subsequent optimal configuration details (e.g., lifting surface shape). This study illustrated that a variety of aerodynamic sources provide the most accurate aerodynamic characterization. Flexible analytical tools accommodate various configurations and enable rapid iteration to alter the configuration for optimization. These analysis techniques drastically reduce the number of configurations that must undergo aerodynamic characterization and determine the optimal flight parameters (e.g., lifting surface characteristics, deflection angle) for flight simulation. Finally, high-fidelity flight simulations are required to obtain the range extension of the gliding indirect fire munition technologies.

This study also identified two driving technologies, lift-to-drag of the overall configuration and the control mechanism that induces the optimal trim angle to the body, which limit the range of gliding indirect fire munitions. Maximizing the lift-to-drag of the configuration subject to constraints (e.g., packaging, survivability, temperature, vibration, and handling) is most critical. Slender bodies (high length-to-diameter, long ogive), boattails, morphing fins to maintain stability while minimizing drag across Mach number, high aspect ratio lifting surfaces with airfoil cross-sections, and technologies to delay stall should be sought. For a given configuration, it is important that the control mechanism (e.g., deflecting canards, fins, wings) be emplaced and sized for the airframe to reach the optimal lift-to-drag.

The aerodynamics feature some uncertainty, which likely grows with angle of attack and influences the recommendations of optimal configuration that result from this analysis approach. Future research should include means of propagating this uncertainty throughout the framework and also focus on improving aerodynamic characterization of maneuvering vehicle configurations, particularly at higher angles of attack where the nonlinear effects are significant. In addition, future work will focus on the technologies to improve lift-to-drag and develop control mechanisms to induce optimal trim angles subject to specific application constraints.

8. References

1. Brown TG, Davis B, Hepner D, Faust J, Myers C, Muller P, Harkins T, Hollis M, Miller C, Placzankis B. Strap-down microelectromechanical (MEMS) sensors for high-G munition applications. IEEE Transactions on Magnetics. 2001;37(1):336–342.

2. Chen M, Berman M, Abrahamian A, Knight R. An experimental and computational study of ball-grid-array printed circuit boards subject to high-acceleration excitations. Aberdeen Proving Ground (MD): Army Research Laboratory (US); 2014. Report No.: ARL-TR-6618.

3. Minnicino M, Sorensen B, Hepner DJ, Horst AW, Schmidt EM, Brandon FJ. Artillery range extension. Aberdeen Proving Ground (MD): Army Research Laboratory (US); 2010. Report No.: ARL-TR-5221.

4. Costello M. Extended range of a gun launched smart projectile using controllable canards. Shock and Vibration. 2001;8:203–213.

5. Fresconi FE. Range extension of gun-launched smart munitions. International Ballistics Symposium; 2008; New Orleans, LA.

6 Fresconi FE, Celmins I, Fairfax L. Optimal parameters for maneuverability of affordable precision munitions. Aberdeen Proving Ground (MD): Army Research Laboratory (US); 2011. Report No.: ARL-TR-5647.

7. Fresconi FE, Harkins T. Experimental flight characterization of asymmetric and maneuvering projectiles from elevated gun firings. Journal of Spacecraft and Rockets. 2012;49(6):1120–1130.

8. Fresconi FE, Brown G, Celmins I, DeSpirito J, Ilg M, Maley J, Magnotti P, Scanlan A, Stout C, Vazquez E. Very affordable precision projectile technology development and flight demonstrations. Aberdeen Proving Ground (MD): Army Research Laboratory (US); 2011. Report No.: ARL-TR-5460.

9. Fresconi FE. Guidance and control of a projectile with reduced sensor and actuator requirements. Journal of Guidance, Control, and Dynamics. 2011;34(6):1757–1766.

10. Fresconi FE, Guidos B, Celmins I, DeSpirito J. Flight behavior of an asymmetric missile through advanced characterization techniques. Journal of Spacecraft and Rockets. 2017;54(1):266–277.

11. McCoy RL. Modern exterior ballistics. Atglen (PA): Schiffer; 2012.

12. Fresconi FE, Celmins I, Silton S, Costello M. High maneuverability projectile flight using low cost components. Aerospace Science and Technology. 2015;41:175–188.

13. Fresconi FE, Celmins I, Maley J, Nelson B. Experimental flight characterization of a canard-controlled, subsonic missile. Aberdeen Proving Ground (MD): Army Research Laboratory (US); 2017. Report No.: ARL-TR-8086.

14. PRODAS User Manual. South Burlington (VT): Arrow Tech Associates Inc.; 2017.

15. Rosema C, Doyle J, Blake W. Missile DATCOM user's manual – 2014 revision. Flight Dynamics Directorate, Wright Patterson Air Force Base (OH), Air Force Research Laboratory (US); 2014. Report No.: AFRL-RQ-WP-TR-2014-0281.

16. Auman LM, Kirby-Brown K. MissileLab user's guide. Redstone Arsenal (AL): Army Aviation and Missile Research, Development, and Engineering Center (US); 2012. Report No.: RDMR-SS-12-08.

17. Aftosmis MJ, Berger MJ, Adomavicius G. A parallel multilevel method for adaptively refined Cartesian grids with embedded boundaries. 38th Aerospace Sciences Meeting and Exhibit; 2000; AIAA paper 2000-0808.

18. Nemec M, Aftosmis M, Pulliam T. CAD-based aerodynamic design of complex configurations using a Cartesian method. 42nd AIAA Aerospace Sciences Meeting and Exhibit; 2004; AIAA paper 2004-0113.

19. Rodriguez DL. Multidisciplinary optimization of a supersonic inlet using a Cartesian CFD method. 10th AIAA/ISSMO Multidisciplinary Analysis and Optimization Conference; 2004; AIAA paper 2004-4492.

20. Nemec M, Aftosmis MJ. Aerodynamic shape optimization using a Cartesian adjoint method and cad geometry. 24th AIAA Applied Aerodynamics Conference; 2006; AIAA paper 2006-3456.

21. Rodriguez DL. Response surface based optimization with a Cartesian CFD method. 41st AIAA Aerospace Sciences Meeting and Exhibit; 2003; AIAA paper 2003-0465.

22. Aftosmis MJ, Nemec M, Cliff SE. Adjoint-based low-boom design with Cart3D. 29th AIAA Applied Aerodynamics Conference; 2011; AIAA paper 2011-3500.

23. Nemec M, Aftosmis MJ. Parallel adjoint framework for aerodynamic shape optimization of component-based geometry. 49th AIAA Aerospace Sciences Meeting; 2011; AIAA paper 2011-1249.

24. Rodrigues DL, Aftosmis MJ, Nemec M, Anderson GR. Optimized off-design performance of flexible wings with continuous trailing-edge flaps. 56th AIAA/ASCE/AHS/ASC Structures, Structural Dynamics, and Materials Conference; 2015; AIAA paper 2015-1409.

25. Anderson GR, Aftosmis MJ. Adaptive shape control for aerodynamic design. 56th AIAA/ASCE/AHS/ASC Structures, Structural Dynamics, and Materials Conference; 2015; AIAA paper 2015-0398.

26. Rodriguez DL, Aftosmis MJ, Nemec M, Anderson GR. Optimization of flexible wings with distributed flaps at off-design conditions. Journal of Aircraft. 2016;53(6).

27. Vasile JD, Fresconi F, Celmins I, Nelson B. Aerodynamic design optimization of control mechanisms for a subsonic, small diameter munition. AIAA/ASCE/AHS/ASC Structures, Structural Dynamics, and Materials Conference; 2018; AIAA paper 2018-1654.

List of Symbols, Abbreviations, and Acronyms

α	angle of attack
$\bar{\alpha}$	$\sqrt{\alpha^2 + \beta^2}$, total angle of attack
β	angle of sideslip
$[\varphi \quad \theta \quad \psi]^T$	body Euler angles for roll, pitch, yaw
δ_F	fin cant angle
ARL	Army Research Laboratory
B	Body
BF	Body-Fin
BFC	Body-Fin-Canard
BFW	Body-Fin-Wing
BFWC	Body-Fin-Wing-Canard
CCDC	US Army Combat Capabilities Development Command
CE	Cartesian Euler
CFD	computational fluid dynamics
CFD	computational fluid dynamics
CG	center of gravity
C_{l_p}	roll damping moment coefficient
C_{l_δ}	static roll moment derivative with respect to control deflection
C_{m_q}	pitch damping moment sum coefficient
C_{m_α}, $C_{m_{\alpha^3}}$	first and third order pitching moment coefficients
C_{N_α}, $C_{N_{\alpha^3}}$	first and third order normal force coefficients
CP	center of pressure
C_{X_0}, $C_{X_{\bar{\alpha}^2}}$	zeroth and second order axial force coefficients
D	diameter
DOD	US Department of Defense
DSRC	DOD Supercomputing Resource Center

L	length
I_{xx}	axial moment of inertia
I_{yy}, I_{zz}	transverse moments of inertia
m	mass
$[p \quad q \quad r]^T$	body angular velocity
PRODAS	Projectile, Rockets, and Ordnance Design and Analysis System
Q	$\frac{1}{2} \rho V^2$, dynamic pressure
S	$D^2\pi/4$, aerodynamic reference area
SEAP	semi-empirical aerodynamic prediction
$[u \quad v \quad w]^T$	body translational velocity
V	velocity
WT	wind tunnel
$[x \quad y \quad z]^T$	Cartesian position of the body center of gravity

1 (PDF)	DEFENSE TECHNICAL INFORMATION CTR DTIC OCA
2 (PDF)	DIR ARL IMAL HRA RECORDS MGMT RDRL DCL TECH LIB
1 (PDF)	GOVT PRINTG OFC A MALHOTRA
12 (PDF)	ARL FCDD RLW F FRESCONI FCDD RLW LE J BRYSON J VASILE I CELMINS P WEINACHT J DESPIRITO FCDD RLW LB N TRIVEDI FCDD RLW LD R BEYER FCDD RLW LC J SADLER FCDD RLW LF M ILG FCDD RLW LG M MINNICINO FCDD RLW LH J NEWILL